Multi-constraint point set registration with redundant point removal for the registration of coronary arteries

Xu, B., Wang, L., Yang, J., Yang, B., Xu, L., Chen, Y. & Zheng, D.

Original citation & hyperlink:
Xu, B, Wang, L, Yang, J, Yang, B, Xu, L, Chen, Y & Zheng, D 2023, 'Multi-constraint point set registration with redundant point removal for the registration of coronary arteries', Computers in Biology and Medicine, vol. 165, 107438.
https://dx.doi.org/10.1016/j.compbiomed.2023.107438

DOI 10.1016/j.compbiomed.2023.107438
ISSN 0010-4825
ESSN 1879-0534

Publisher: Elsevier

Multi-constraint Point Set Registration with Redundant Point Removal for the Registration of Coronary Arteries

Bu Xu [a], Lu Wang [b], Jinzhong Yang [a], Benqiang Yang [a, c], Lisheng Xu [a, d, e, *], Yang Chen [f], and Dingchang Zheng [g]

[a] *College of Medicine and Biological Information Engineering, Northeastern University, Shenyang 110169, China*
[b] *School of Computer Science and Engineering, Northeastern University, Shenyang 110169, China*
[c] *Department of Radiology, General Hospital of North Theater Command, Shenyang 110016, China*
[d] *Key Laboratory of Medical Image Computing, Ministry of Education, Shenyang 110169, China*
[e] *Engineering Research Center of Medical Imaging and Intelligent Analysis, Ministry of Education, Shenyang 110169, China*
[f] *School of Computer Science and Engineering, Southeast University, Nanjing 210096, China*
[g] *Research Centre of Intelligent Healthcare, Coventry University, Coventry CV1 5RW, United Kingdom*

ARTICLE INFO

Keywords:
Point set registration
Coronary arteries
Non-rigid
Multi-constraint
Missing data

A B S T R A C T

Background: Coronary artery disease (CAD) is the leading cause of death worldwide. The registration of the coronary artery at different phases can help radiologists explore the motion patterns of the coronary artery and assist in the diagnosis of CAD. However, there is no automatic and easy-to-execute method to solve the missing data problem that occurs at the endpoints of the coronary artery tree. This paper proposed a non-rigid multi-constraint point set registration with redundant point removal (MPSR-RPR) algorithm to tackle this challenge.
Methods: Firstly, the MPSR-RPR algorithm roughly registered two coronary artery point sets with the pre-set smoothness regularization parameter and Gaussian filter width value. The moving coherent, local feature, and the corresponding relationship between bifurcation point pairs were exploited as the constraints. Next, the spatial geometry information of the coronary artery was utilized to automatically recognize the vessel endpoints and to delete the redundant points of the coronary artery. Finally, the algorithm continued carrying out the multi-constraint registration with another group of the pre-set parameters to improve the alignment performance.
Results: The experimental results demonstrated that the MPSR-RPR algorithm achieved a significantly lower mean value of the modified Hausdorff distance (MHD) compared to the other state-of-the-art methods for addressing the serious missing data in the left and right coronary arteries.
Conclusion: This study demonstrated the effectiveness of the proposed algorithm in aligning coronary arteries, providing significant value in assisting in the diagnosis of coronary artery and myocardial lesions.

1. Introduction

Coronary artery disease (CAD) is the leading cause of mortality in the world [1,2]. The alignment of the coronary artery tree plays a crucial role in cardiovascular research and has many applications. These include estimating the heart motion [3,4], exploring the motion pattern of coronary arteries [5–7], and assisting doctors in diagnosing CAD [8,9].

Point set registration is a valuable tool for matching vascular trees. The registration aims to calculate the corresponding relationship and estimate the deformation between two point sets. Based on the nature of the data, the alignment can be categorized into rigid and non-rigid registration. Rigid registration is relatively straightforward, and the representative approach is the iterated close point (ICP) algorithm [10] and the ICP's derivative methods [11,12]. Compared to rigid registration, non-rigid registration is more challenging. This is because the true non-rigid transformation is usually unknown, and it need to design a more complex algorithm to accurate modeling the non-rigid matching. Myronenko et al. [13,14] introduced the coherent point drift (CPD) method with the Gaussian mixture model (GMM) framework. It considered the motion coherence theory (MCT) [15] of the point set as the global constraint to enforce the smoothness of the displacement field. However, despite its widespread use, the CPD algorithm assumes no specific point correspondence and does not fully utilize the local structure information of the point set. To overcome the limitation, the landmark-guided CPD (LGCPD) algorithm [16] integrates the anatomical landmarks information as a constraint within the CPD method. The LGCPD method has been successfully applied to align the liver and brain vessels, demonstrating improved alignment accuracy compared to the CPD approach. In recent studies, researchers have focused on utilizing both the global constraint and local structure information of the point set to improve registration performance [17–19]. The coronary artery adheres to the heart surface and follows the heart making the complex non-rigid twisting motion. Point set registration has been employed for aligning the coronary artery tree. The registration usually needs to match points that represent the vessels (e.g., points on the vessel centerline) in the different modalities or times. In the percutaneous coronary intervention, some researchers have aligned coronary arteries in 2D X-ray angiography and 3D coronary computed tomography angiography (CCTA) to complement the 3D vascular information [21, 22]. These approaches perform a rigid registration firstly, to compare and analyze the vascular structure in both modalities. Subsequently, non-rigid registration is implemented to realize real-time alignment. Due to the advantages of being non-invasive and cost-effective, CCTA has been widely utilized for the detection of CAD. Some works are based only on the CCTA [5, 6, 7, 8, 9, 23, 24]. The CPD approach has been employed to label the coronary artery branches with their anatomical

* Corresponding author:
Lisheng Xu, PhD
E-mail address: xuls@bmie.neu.edu.cn.

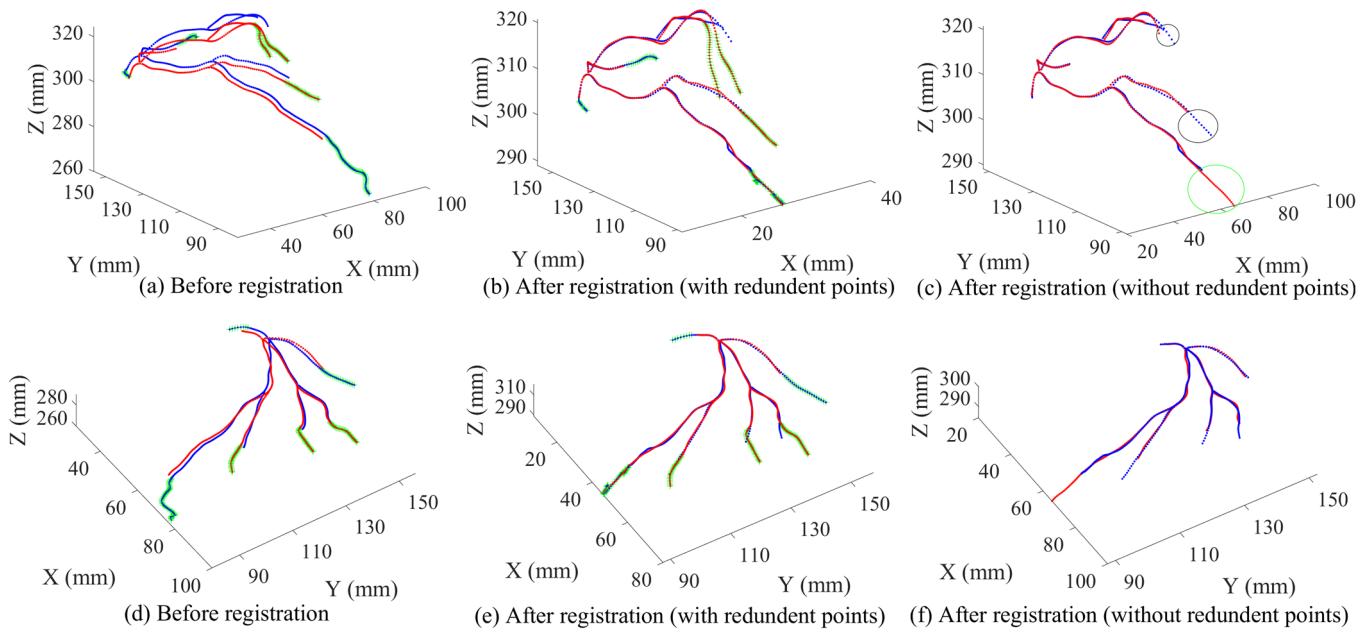

Fig. 1. Illustration of the challenges caused by redundant points. (a) Point set before alignment. The blue point is the moving point set. The red point denotes the target point set, and the green and cyan '+' represents the redundant points. (b) shows the two point sets after the alignment. (c) shows the two point sets after the alignment, which removes redundant points manually. (d), (e), (f) present the (a), (b), (c) from another view angle. The black circles show that because of the redundant points, the points in the moving point set are elongated (i.e., inaccurate registration). The green circle shows that because of the redundant points, the points in the moving point set are squeezed (i.e., inaccurate registration).

names [8] and study the long-term plaque change in coronary arteries [9], therefore, facilitating the diagnosis of CAD. Habert et al. [6] improved the CPD method with the assumption that the movement field of coronary arteries between two consecutive times should be similar. The point set similarity model (PSSM) [23] introduced a new registration framework. It first divides the coronary artery into branches according to the bifurcation. Then, the PSSM calculates the similarity invariant signature curve of each branch and identifies similar branches at two time-points. Finally, optimal transformation is achieved through the linear least square parameter estimation. However, the PSSM algorithm is not suitable for the coronary artery tree with large non-rigid deformation [23].

One of the biggest challenges in the registration of vascular structure is the missing data problem [24,25], as shown in Fig. 1. The aforementioned registration algorithm (e.g., [23]) does not employ a specific strategy to solve the missing data problem. Due to the variation in seed points used for extracting centerline point sets of coronary arteries, some degree of missing data always occurs at the end of branches. Points in one set that lack corresponding points in another set are regarded as redundant points. In [5], a registration method that combines the information of points on the centerline and vessel bifurcation was proposed to track the motion of the coronary arteries in CCTA throughout the whole cardiac cycle. The missing data problem was addressed by removing redundant points manually [5]. In another study by Zeng et al. [24], after aligning the vessel point sets obtained through thresholding and region-growing segmentation, the level set method was utilized for two rounds of coronary artery segmentation in the CCTA images to reduce the number of redundant points. After the re-segmentation process, the registration was executed again, resulting in improved registration accuracy. However, the method in [24] is time-consuming due to re-segmentation and re-registration steps, especially when dealing with many vessel branches with missing data.

As of now, no automatic and easy-to-execute method has been developed to effectively address the issue of the missing data problem that appears at the endpoints of the coronary artery tree. Therefore, this paper aims to tackle this challenge by proposing a multi-constraint point set registration with redundant point removal (MPSR-RPR) algorithm. The proposed method considered registration as a maximum likelihood estimation (MLE) problem. It incorporated the motion coherence as a global constraint, combined the shape context and nearest neighbor information of the point set to assign mixing coefficients, and introduced bifurcation pairs information to improve the matching performance. A strategy for identifying and removing redundant points was also devised. The expectation-maximization (EM) method was employed to solve the MLE. In the E-step, the corresponding relationship between the two point sets was obtained, while in the M-step, the non-rigid transformation parameters were calculated. The proposed method is automatic and easy to use, and its performance was compared with the state-of-the-art alignment approaches.

The rest of the paper is organized as follows. Section 2 presents the details of the MPSR-RPR algorithm. Section 3 describes the dataset and evaluation metrics used in this study. Section 4 presents the qualitative and quantitative experiment results. The discussion and conclusion of the paper are given in section 5 and section 6, respectively.

2. Methods

2.1 Multi-constraint Point Set Registration (MPSR)

GMM is the superposition of multiple single Gaussian models. From the perspective of statistics, no matter how the observation data is distributed, GMM can be used to fit the probability density function of the data set with high accuracy. For the non-rigid point set alignment, the moving point set $\boldsymbol{Y}_{M\times 3} = (\boldsymbol{y}_1,\cdots,\boldsymbol{y}_M)^T$ is regarded as the centroids of the GMM, while the target point set $\boldsymbol{X}_{N\times 3} = (\boldsymbol{x}_1,\cdots,\boldsymbol{x}_N)^T$ is considered as the data points of the GMM. Suppose there are L bifurcation point pairs, and their coordinates are represented by $\boldsymbol{Y}^*_{L\times 3} = (\boldsymbol{y}^*_1,\cdots,\boldsymbol{y}^*_L)^T$, and $\boldsymbol{X}^*_{L\times 3} = (\boldsymbol{x}^*_1,\cdots,\boldsymbol{x}^*_L)^T$. The aim is to warp $\boldsymbol{Y}$ onto $\boldsymbol{X}$. Let $\mathcal{T}(\boldsymbol{Y}) = \boldsymbol{Y} + v(\boldsymbol{Y})$ represents the deformed point set of $\boldsymbol{Y}$, where v is the displacement field between $\boldsymbol{Y}$ and $\mathcal{T}(\boldsymbol{Y})$. Assume the isotropy of GMM with variance σ^2 and considering the outliers in the point set satisfies the uniform distribution $\frac{1}{V}$, where V is the volume of the smallest bounding box containing the point set. The probability density function of $\boldsymbol{x}_n$ is in the form:

$$p(\boldsymbol{x}_n) = \omega\frac{1}{V} + (1-\omega)\sum_{m=1}^{M}\frac{\pi_{mn}}{(2\pi\sigma^2)^{3/2}}\exp\left(-\frac{\|\boldsymbol{x}_n - \mathcal{T}(\boldsymbol{y}_m)\|^2}{2\sigma^2}\right), \qquad (1)$$

where π_{mn} denotes the mixing coefficients. $\omega(0 \le \omega \le 1)$ represents the weight value. The negative log-likelihood function of the data points takes the form:

$$E(v,\sigma^2) = -\sum_{n=1}^{N} \ln p(\boldsymbol{x}_n). \tag{2}$$

By solving the minimization problem of Eq. (2), the alignment parameters can be estimated. Further, considering the deformed point set satisfies the motion coherence [15], this prior knowledge is exploited as the global constraint to enforce the smoothness of the v. Then, Eq. (2) is rewritten as:

$$E(v,\sigma^2) = -\sum_{n=1}^{N} \ln p(\boldsymbol{x}_n) + \frac{\lambda}{2}\phi(v), \tag{3}$$

where $\phi(\cdot)$ is the high-pass filtering function, and it is utilized to estimate the "oscillatory" degree of v. λ represents the weight parameter. For the minimization problem of Eq. (3), the EM approach is adopted to estimate the registration parameters.

E-step: Suppose the "old" parameters $[\mathcal{T}(\boldsymbol{Y})]^{old}$ and σ^{old} are known, then the corresponding relationships between $[\mathcal{T}(\boldsymbol{y}_m)]^{old}$ and $\boldsymbol{x}_n$ is calculated by

$$p_{mn} = \frac{\pi_{mn} \exp(-\frac{\|\boldsymbol{x}_n - [\mathcal{T}(\boldsymbol{y}_m)]^{old}\|^2}{2(\sigma^{old})^2})}{\sum_{k=1}^{M} \pi_{kn} \exp(-\frac{\|\boldsymbol{x}_n - [\mathcal{T}(\boldsymbol{y}_k)]^{old}\|^2}{2(\sigma^{old})^2}) + (2\pi(\sigma^{old})^2)^{3/2} \frac{\omega}{V(1-\omega)}}. \tag{4}$$

Let $\boldsymbol{P} = [p_{mn}]_{M\times N}$ represents the a posteriori probability matrix. Motion coherence constraint is the global-structure constraint, the local-structure constraint can also help to decrease the registration error [26]. In this paper, the 3D shape context [27] is exploited as the local feature descriptor to obtain the local information of the deformed and target point set, respectively. By using the Hungarian algorithm, the corresponding relationships between the two point sets are obtained. Then, the mixing coefficients are assigned by

$$\pi_{mn} = \begin{cases} \frac{\tau+1}{M+\tau}, \text{if } [\mathcal{T}(\boldsymbol{y}_m)]^{old} = [\mathcal{T}(\boldsymbol{y}_k)]^{old} \\ \frac{1}{M+\tau}, \text{if } [\mathcal{T}(\boldsymbol{y}_m)]^{old} \neq [\mathcal{T}(\boldsymbol{y}_k)]^{old} \end{cases}, \tag{5}$$

$$\tau = \frac{2}{\exp(0.5 * Dist) - 1 + c}, \tag{6}$$

where $[\mathcal{T}(\boldsymbol{y}_k)]^{old}$ is the corresponding point of $\boldsymbol{x}_n$ which is obtained by the Hungarian algorithm, and $c = 10^{-7}$ is a disturbance term. Let $K_{[\mathcal{T}(\boldsymbol{y}_m)]^{old}}$ and $K_{\boldsymbol{x}_n}$ denote the 10 nearest neighbors of $[\mathcal{T}(\boldsymbol{y}_m)]^{old}$ and $\boldsymbol{x}_n$, respectively. $Dist$ is the Euclidean distance between the mean value of $K_{[\mathcal{T}(\boldsymbol{y}_m)]^{old}}$ and the mean value of $K_{\boldsymbol{x}_n}$. If there is no corresponding point for $\boldsymbol{x}_n$, the equal mixing coefficients will be used, i.e., $\pi_{mn} = \frac{1}{M}, \forall m \in [1, M]$.

M-step: Based on the $\boldsymbol{P}$ that was obtained at the E-step, ignoring the constants independent term of v and σ^2, Eq. (3) is rewritten as:

$$Q(v,\sigma^2) = \frac{1}{2\sigma^2}\sum_{n=1}^{N}\sum_{m=1}^{M} p_{mn} \| \boldsymbol{x}_n - (\boldsymbol{y}_m + v(\boldsymbol{y}_m)) \|^2 + \frac{3N_p}{2}\ln\sigma^2 + \frac{\lambda}{2}\phi(v), \tag{7}$$

where $N_p = \sum_{n=1}^{N}\sum_{m=1}^{M} p_{mn}$. Further, the corresponding relationship of vessel bifurcation point is exploited as prior knowledge. The joint probability of the bifurcation point pairs is in the form [16]:

$$\prod_{l=1}^{L} \frac{1}{(2\pi(\sigma^*)^2)^{3/2}} \exp(-\frac{\|\boldsymbol{x}_l^* - (\boldsymbol{y}_l^* + v(\boldsymbol{y}_l^*))\|^2}{2(\sigma^*)^2}), \tag{8}$$

where σ^* is used to control the influence of the bifurcation point pairs. Calculating the negative logarithm of (8), taking it as the constraint, and integrating it into the Eq. (7), then obtains

$$\begin{aligned} Q'(v,\sigma^2) &= \frac{1}{2\sigma^2}\sum_{n=1}^{N}\sum_{m=1}^{M} p_{mn} \| \boldsymbol{x}_n - (\boldsymbol{y}_m + v(\boldsymbol{y}_m)) \|^2 + \frac{3N_p}{2}\ln\sigma^2 + \frac{\lambda}{2}\phi(v) \\ &\quad + \frac{1}{2(\sigma^*)^2}\sum_{l=1}^{L} \| \boldsymbol{x}_l^* - (\boldsymbol{y}_l^* + v(\boldsymbol{y}_l^*)) \|^2 \\ &= \frac{1}{2\sigma^2}\sum_{j=1}^{N+L}\sum_{i=1}^{M+L} p'_{ij} \| \boldsymbol{x}'_j - (\boldsymbol{y}'_i + v(\boldsymbol{y}'_i)) \|^2 + \frac{3N_p}{2}\ln\sigma^2 + \frac{\lambda}{2}\phi(v), \end{aligned} \tag{9}$$

where $p'_{ij} = \begin{cases} p_{mn}, & (i = m, m \in [1, M]) \text{ and } (j = n, n \in [1, N]) \\ \sigma^2/(\sigma^*)^2, & (i = M + l) \text{ and } (j = N + l), l \in [1, L] \\ \mathbf{0}, & \text{otherwise} \end{cases}$. Let

$$\boldsymbol{P}' = [p'_{ij}]_{(M+L)\times(N+L)} = \begin{bmatrix} [p_{mn}]_{M\times N} & \mathbf{0} \\ \mathbf{0} & \frac{\sigma^2}{(\sigma^*)^2}\cdot\mathbf{I}_L \end{bmatrix}, \tag{10}$$

$$\boldsymbol{X}' = [\boldsymbol{x}'_j]_{(N+L)\times 3} = [[\boldsymbol{x}_n]_{N\times 3}; [\boldsymbol{x}_l^*]_{L\times 3}], \tag{11}$$

$$\boldsymbol{Y}' = [\boldsymbol{y}'_i]_{(M+L)\times 3} = [[\boldsymbol{y}_m]_{M\times 3}; [\boldsymbol{y}_l^*]_{L\times 3}]. \tag{12}$$

The centroids and variance can be updated by solving the minimization problem for Eq. (9). By using the variational calculus, the functional form of v is formed as [13]:

$$v(\boldsymbol{y}') = \sum_{k=1}^{M+L} \boldsymbol{w}_k \boldsymbol{G}(\boldsymbol{y}', \boldsymbol{y}'_k), \tag{13}$$

where $\boldsymbol{G}(\boldsymbol{y}'_i, \boldsymbol{y}'_j) = \exp(-\frac{\|\boldsymbol{y}'_i - \boldsymbol{y}'_j\|^2}{2\beta^2})$ is the element of the Gaussian kernel matrix with the Gaussian filter width β, $\boldsymbol{w}_k$ denotes the weight coefficient. Let $\boldsymbol{W}_{(M+L)\times 3} = (\boldsymbol{w}_1, \mathrm{L}, \boldsymbol{w}_{M+L})^T$ represents the coefficient matrix. Then, it has $\phi(v) = Tr(\boldsymbol{W}^T \boldsymbol{G} \boldsymbol{W})$, where $Tr(\cdot)$ is the trace of the matrix. Taking Eq. (13) back into Eq. (9) and calculating $\frac{\partial Q'}{\partial \boldsymbol{W}} = \mathbf{0}$, it obtains

$$(\boldsymbol{G} + \lambda\sigma^2 d(\boldsymbol{P}'\mathbf{1})^{-1})\boldsymbol{W} = d(\boldsymbol{P}'\mathbf{1})^{-1}\boldsymbol{P}'\boldsymbol{X}' - \boldsymbol{Y}', \tag{14}$$

where $d(\cdot)$ denotes the diagonal matrix. Therefore, it has $\mathcal{T}(\boldsymbol{Y}') = \boldsymbol{Y}' + v(\boldsymbol{Y}') = \boldsymbol{Y}' + \boldsymbol{G}\boldsymbol{W}$.

Taking $\frac{\partial Q'}{\partial \sigma^2} = \mathbf{0}$, it obtains

$$\sigma^2 = \frac{1}{3N_p}\sum_{n=1}^{N}\sum_{m=1}^{M} p_{mn} \| \boldsymbol{x}_n - (\boldsymbol{y}_m + v(\boldsymbol{y}_m)) \|^2. \tag{15}$$

To achieve the registration between $\boldsymbol{Y}$ and $\boldsymbol{X}$, the E-step and M-step need to be executed repeatedly.

2.2 Removal Strategy for Redundant Points

The point set matching method is adopted to study the motion of the coronary artery. Because of the position difference of the seed points when extracting the point set of the coronary artery centerline, there is always a missing vessel segment at the end of the vessel branch. Although the registration method in 2.1 exploits the motion coherence, local feature, and the bifurcation points information of the vessel point set, it is still affected by the missing data problem. Many registration methods consider the motion smoothness of the point set as the most important prior constraint. Therefore, the smoothness regularization parameter λ and the Gaussian filter width β play an important role in these methods. In this paper, an automatic removal strategy for the redundant points was proposed to improve the alignment accuracy of the coronary artery. The pseudo-code of the whole algorithm is shown in Tab. 1.

The proposed removal strategy is as the following four steps:

Step 1: Carrying out the registration algorithm in 2.1 with a large λ and β (e.g., $\lambda = 10, \beta = 5$), until the number of iterations reaches the pre-set value, and this step is called the rough matching of two centerline point sets.

Step 2: Automatic identification of endpoints for coronary point sets.

(1) Based on the registration result in Step 1, traversing all the points in the deformed point set $(\mathcal{T}(\boldsymbol{y}_1), \cdots, \mathcal{T}(\boldsymbol{y}_M))^T$, making a cube centered at the current point, and the points contained in the cube are regarded as the neighbor points of the current point. Let $\mathcal{T}(\boldsymbol{y}_i)$ denotes the current point, and suppose there are K_i points in the cube centered at $\mathcal{T}(\boldsymbol{y}_i)$. The $K_i - 1$ neighbor points are denoted by $(\mathcal{T}(\boldsymbol{y}_{i1}), \cdots, \mathcal{T}(\boldsymbol{y}_{i(K_i-1)}))^T$.

(2) Calculating the Euclidean distance between the current point $\mathcal{T}(\boldsymbol{y}_i)$ and its neighbors, therefore, the nearest neighbor (let $\mathcal{T}(\boldsymbol{y}_{i1})$ represents the nearest neighbor) of the current point is found. Taking $\mathcal{T}(\boldsymbol{y}_i)$ as the start point and $\mathcal{T}(\boldsymbol{y}_{i1})$ as the end point, the base vector $\boldsymbol{u}_{i1}$ can be obtained. Then, taking $\mathcal{T}(\boldsymbol{y}_i)$ as the start point and the other points in $(\mathcal{T}(\boldsymbol{y}_{i2}),\cdots,\mathcal{T}(\boldsymbol{y}_{i(K_i-1)}))^T$ as the end point to get the vector respectively, and calculating the Cosine value:

$$Cos < \boldsymbol{u}_{i1}, \boldsymbol{u}_{ik} >, i = 1,\cdots,M \ and \ k = 2,\cdots,(K_i - 1). \quad (16)$$

If there is one of the $Cos < \boldsymbol{u}_{i1}, \boldsymbol{u}_{ik} >, k = 2,\mathrm{L}\ ,(K_i - 1)$ values smaller than zero, the current point $\mathcal{T}(\boldsymbol{y}_i)$ will be judged as the intermediate point. Otherwise, the current point will be identified as the endpoint of the vessel point set, and the 2D geometric illustration is shown in Fig. 2. In the same way, all the endpoints for the target point set can be identified.

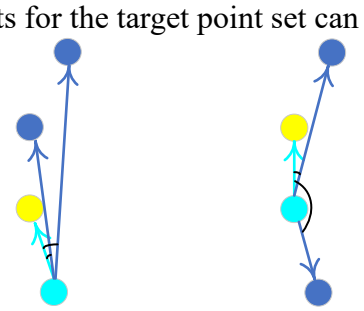

(a) Endpoint (b) Intermediate point

Fig. 2. The 2D geometric interpretation for judgment of the endpoint and intermediate point of the centerline point set. The cyan point represents the current point, the yellow point is the nearest point of the current point, and the blue points are the other neighbors. If there is a Cosine value of the angle between the base vector (i.e., the cyan line) and the ordinary vector (i.e., the blue line) is smaller than zero, it represents the current point is the intermediate point; otherwise, it's the endpoint of the vessel.

Step 3: Deleting the redundant points.

Let $E_m = [e_{m1},\cdots,e_{mS}]$ and $E_t = [e_{t1},\cdots,e_{tS}]$ represent the endpoints that are identified of the deformed and target point set respectively, where S is the number of the vessel endpoint. Let $D = [d_1(e_{m1},e_{t1}),\cdots,d_S(e_{mS},e_{tS})]$ denotes the Euclidean distance between the corresponding endpoints Taking two corresponding endpoints, for example, the e_{ms} and e_{ts}, as the center of two spheres and their distance $d_s(e_{ms},e_{ts})$ as the radius, two spheres can be generated. Counting the number of points in the two spheres respectively, and denoting them by n_{ms} and n_{ts}. If $n_{ms} < n_{ts}$, then deleting all the points belonging to the deformed point set in the sphere which centers at e_{ms}; else deleting all the points belonging to the target point set in the sphere which centers at e_{ts}. Fig. 3 explains the removal principle. Executing this process for all the S corresponding endpoint pairs.

Especially, when two branches of a vessel are very close to each other, the current sphere can easily contain the points on the adjacent branch of the same vessel, as shown in Fig. 3 (d). However, deleting the points on the adjacent branch is not expected. Therefore, the "distance mutation" method is utilized, to judge whether the set of points in the sphere comes from the same branch of a vessel. Specifically,

(1) Calculating the distance between every two points belonging to the same kind (deformed or target) of point set in a sphere, taking the endpoint as the current point $e_{current}$, finding the nearest neighbor $e_{nearest}$ of $e_{current}$, and saving the distance d_{old} between the $e_{current}$ and $e_{nearest}$;

(2) Taking the $e_{nearest}$ as the current point, and finding the nearest neighbor for $e_{current}$ in the sphere (the used points will not be searched repeatedly). The Euclidean distance between $e_{current}$ and $e_{nearest}$ is denoted as d_{new}. If $d_{new} > 3d_{old}$, it represents the points that have not been searched are on the adjacent branch, therefore, these points will not be deleted; else, carrying out (2) repeatedly, until all the points belonging to the same kind of point set in the sphere are searched.

Step 4: After the removal, continue to carry out the registration method with a small λ and β (e.g., $\lambda = 1, \beta = 1$), until the termination conditions are satisfied, which is called the fine registration process.

Tab. 1. Pseudo-code of the MPSR-RPR approach

Input: Two point sets $\boldsymbol{Y}$ and $\boldsymbol{X}$, the point sets with bifurcation $\boldsymbol{Y}'$ and $\boldsymbol{X}'$, parameters λ_{tough}, β_{tough}, λ_{fine}, β_{fine}, pre_iter, ω, σ^*.
Output: The optimal transformation $\mathcal{T}$.
Initialization: $\boldsymbol{W} = \boldsymbol{0}$, $\sigma^2 = \frac{1}{3NM}\sum_{m,n=1}^{M,N} \| \boldsymbol{x}_n - \boldsymbol{y}_m \|^2$, $iter = 0$;
Construct $\boldsymbol{G}$: $g_{ij} = \exp(-\frac{\|\boldsymbol{y}_i' - \boldsymbol{y}_j'\|^2}{2(\beta_{tough})^2})$;
Repeat until Q converges
  If $iter = pre\_iter$
    Recognize the endpoint by Eq. (16);
    Remove the redundant points according to the generated sphere;
    Update $\mathcal{T}(\boldsymbol{Y})$, $\boldsymbol{X}$, $\boldsymbol{Y}'$, $\boldsymbol{X}'$, $\boldsymbol{G}$, and $\boldsymbol{W}$ according to the removal;
  Compute feature descriptors for the point set $\boldsymbol{X}$;
  E-step:
    Compute feature descriptors for the point set $[\mathcal{T}(\boldsymbol{Y})]^{old}$;
    Assign π_{mn} based on the feature correspondence;
    Calculate a *posteriori* probability matrix $\boldsymbol{P}$ by Eq. (4);
  M-step:
    Update $\boldsymbol{W}$ by solving Eq. (14);
    Update $\mathcal{T}(\boldsymbol{Y}') = \boldsymbol{Y}' + \boldsymbol{GW}$;
    Update σ^2 by Eq. (15);
  $iter = iter + 1$;
The transformation $\mathcal{T}$ is determined as $\mathcal{T}(\boldsymbol{Y}') = \boldsymbol{Y}' + \boldsymbol{GW}$.

3. Experiments

3.1 Dataset

The CCTA data of sixteen subjects were obtained from the General Hospital of North Theater Command. Each data contains ten time-points

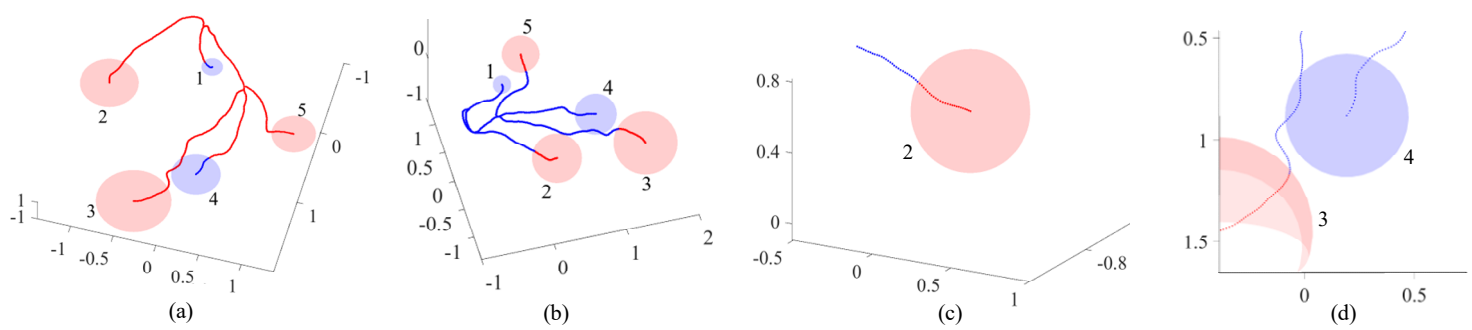

(a) (b) (c) (d)

Fig. 3. The removal principle for the redundant points that appear at the end of the vessel branch. After the rough registration, the blue point set (i.e., the deformed point set) was warped onto the red point set (i.e., the target point set). In (a) which view is (96, 85), the blue points in spheres 1 and 4 are the redundant points for the deformed point set. In (b) which view is (-11, 53), the red points in spheres 2, 3, and 5 are the redundant points for the target point set. (c) shows the local magnification of sphere 2. (d) presents the local magnification of sphere 4, and it shows the situation that sphere 4 includes the points on the adjacent branch of the same coronary artery.

(i.e., 00, 10, …, 90 phases) coronary arteries image in a complete cardiac cycle, allowing to align the point set of the coronary artery centerline between the adjacent time-points. The software Mimics was used to segment the vessels, extract and reconstruct the centerline point sets. Because of the position difference of the seed points when extracting the centerline for the vessels, there is always missing data appears at the end of the vessel branch. Fig. 4 shows the statistical results for the missing percentage of the extracted real vessels, and a total of 1240 pairs of vascular branches have been counted. From Fig. 4, it can be found that the missing percentage between the real branches is mostly distributed under 50%.

To quantify the performance of the proposed algorithm, according to the displacement and deformation degree of the real vessels between the adjacent phases, 16 simulation data (each data contains the coronary centerlines at 00, ..., 90 phases) was constructed by using the Gaussian radial basis function [28], and one of the simulation data is shown in Fig. 5. Because of the existence of the missing data on the real vessel branches, 10%, 20%, 30%, or 40% missing at the end of branches between two adjacent phases on 16 simulation data was constructed [1], respectively. The details for constructing the missing data are as follows: (1) for the vessel point sets between two adjacent phases, according to the bifurcation points, the two vessel point sets were divided into several branches; (2) counting the number of points in the branches that include the endpoint of the vessel, respectively; (3) at the end position of the arteries, the fixed ratio (e.g., 10%) points of the branch was removed to simulate the missing data. 10% missing and 40% missing at the end of branches are illustrated in Fig. 5 (c) and (d), respectively.

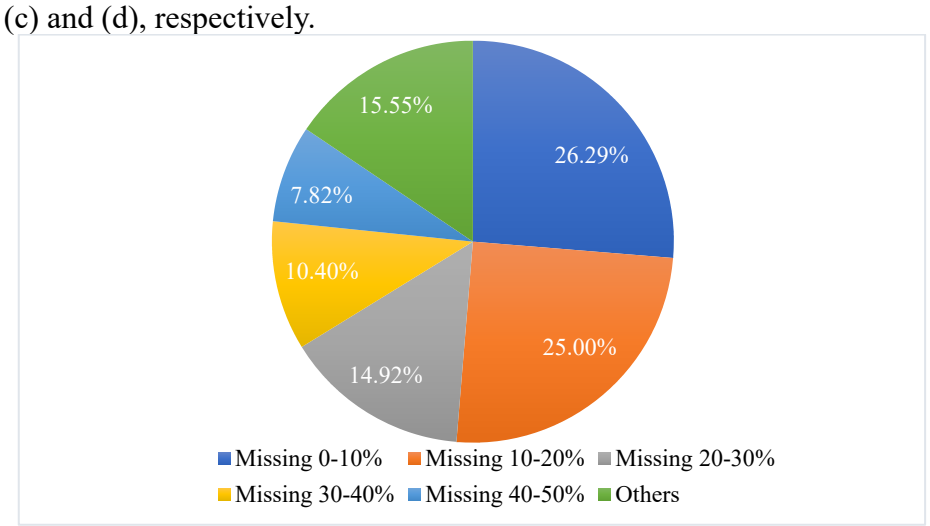

Fig. 4. The statistical results of the missing percentage of real coronary arteries in this study

3.2 Implementation Details

In the MPSR-RPR algorithm, λ_{tough}=10 , β_{tough}=5 , λ_{fine}=1 , β_{fine}=1 , σ^{*}=10^{-4} , and ω=0.05 was utilized. The iteration number for the parameter change was set to pre_iter=40 . The proposed MPSR-RPR approach was quantitatively compared with the CPD [14], LGCPD [16], and Hausdorff-distance-guided point set registration (HDPSR) [19] algorithm on 16 simulation data. To verify the effect of the removal, the proposed redundant removal strategy was also integrated into the CPD, LGCPD, and HDPRS algorithms. Calling them the CPD-RPR, LGCPD-RPR, and HDPSR-RPR, respectively. Further, only changing the rough and fine matching parameters without the removal were experimented, and these methods were called the CPD-para, LGCPD-para, HDPSR-para, and MPSR-para, respectively. In total, 12 methods were compared, i.e., the CPD, LGCPD, HDPSR, MPSR, CPD-para, LGCPD-para, HDPSR-para, MPSR-para, CPD-RPR, LGCPD-RPR, HDPSR-RPR, and MPSR-RPR algorithms.

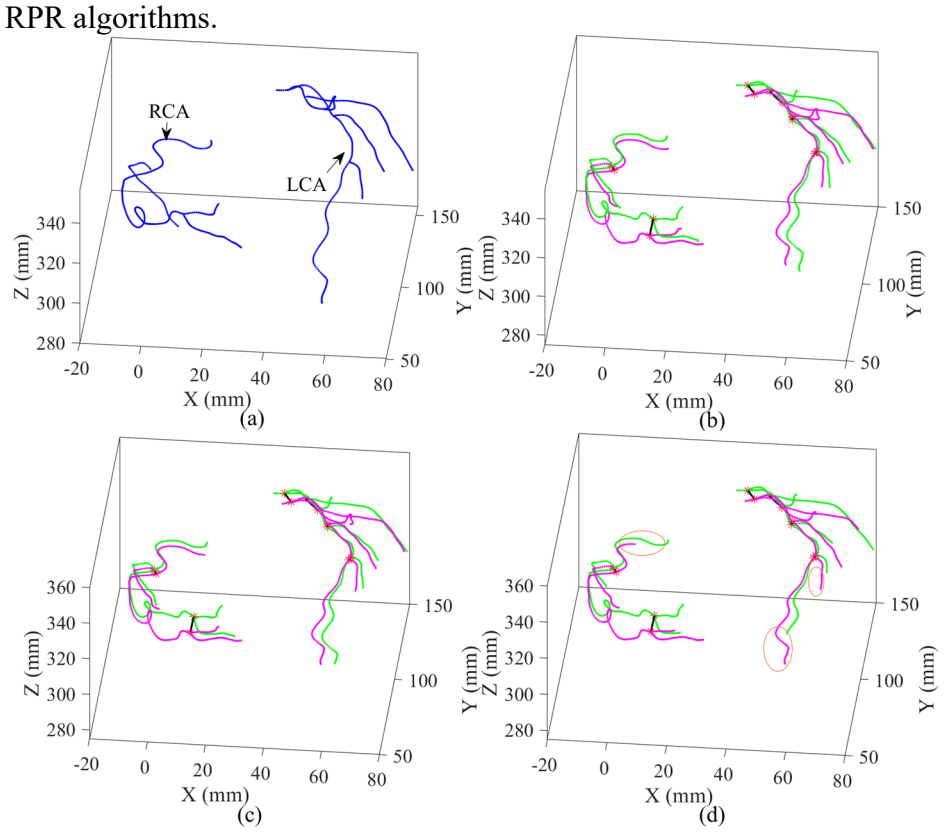

Fig. 5. Point sets of the coronary centerline. (a) Point set of the left coronary artery (LCA) and right coronary artery (RCA) at 00 (■) phase. (b) Simulated point sets at 10 (■), and 20 (■) phases. (c) 10% missing between 10 and 20 phases. (d) 40% missing between 10 and 20 phases. The red star represents the bifurcation of the coronary arteries. The black line denotes the corresponding relationship between the bifurcations of two adjacent phases. The orange circle illustrates that (d) has a larger missing degree than (c) at the corresponding position.

3.3 Evaluation metrics

The performance of these 12 methods was compared using the criteria standard from the modified Hausdorff distance (MHD) [29]:

$$dist(\boldsymbol{y}, \boldsymbol{B}) = \min_{\boldsymbol{b}\in\boldsymbol{B}} \| \boldsymbol{y} - \boldsymbol{b} \|, \tag{17}$$

$$d^{*}(\boldsymbol{Y}_{final}, \boldsymbol{B}) = \frac{1}{M_{new}} \sum_{\boldsymbol{y}\in\boldsymbol{Y}_{final}} dist(\boldsymbol{y}, \boldsymbol{B}), \tag{18}$$

$$f(d^{*}(\boldsymbol{Y}_{final}, \boldsymbol{B}), d^{*}(\boldsymbol{B}, \boldsymbol{Y}_{final})) = \max(d^{*}(\boldsymbol{Y}_{final}, \boldsymbol{B}), d^{*}(\boldsymbol{B}, \boldsymbol{Y}_{final})), \tag{19}$$

where $\boldsymbol{Y}_{final}$ is the final moving point set after the registration, M_{new} is the number of points in $\boldsymbol{Y}_{final}$, $\boldsymbol{B}$ represents the point set of the ground truth, and f denotes the MHD.

The smaller MHD corresponds to the higher accuracy of the registration method. For the 16 simulated data, the mean and standard deviation of MHD for adjacent phases was first calculated across all the phases. Next, the difference in the MHD mean value between the two algorithms at each of the adjacent phases was calculated. The range of the difference was obtained to compare the performance of the two methods. In addition, the total running time (for 16×10 adjacent phases) for each of the registration methods was calculated and compared.

4. Results

Fig. 6 and Fig. 7 show the MHD for the LCA and RCA with different degrees of missing data (10%, 20%, 30%, and 40%). It can be seen that only with the parameters (i.e., λ and β) change, the MHD reduced for

[1] https://github.com/abcxubu/Dataset-of-vascular-tree-point-set

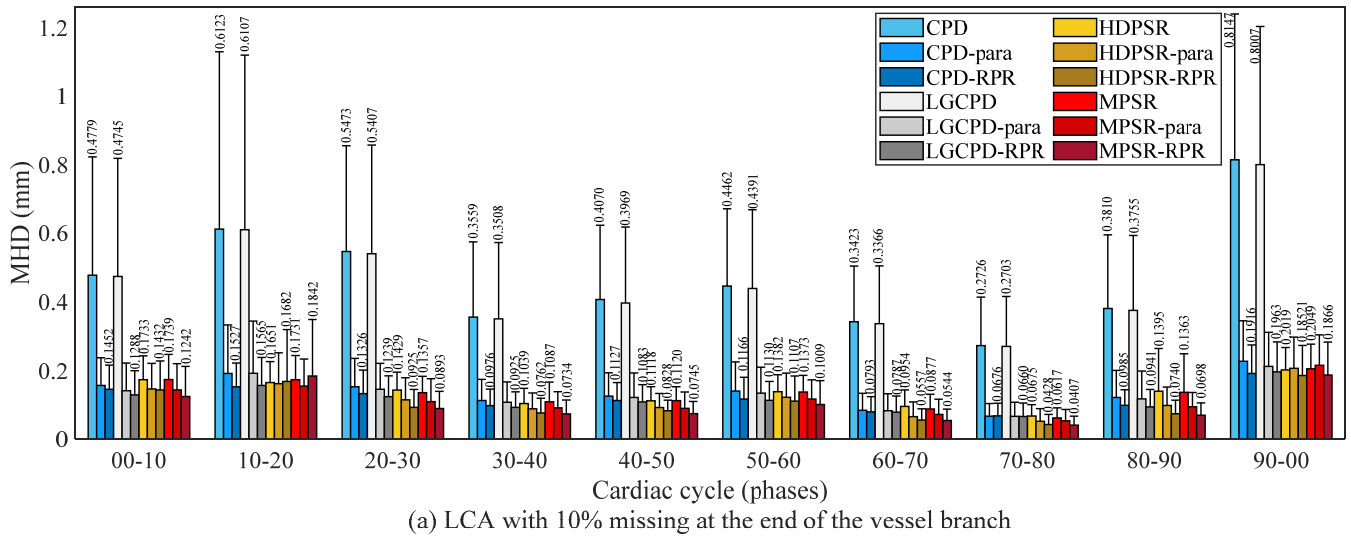

(a) LCA with 10% missing at the end of the vessel branch

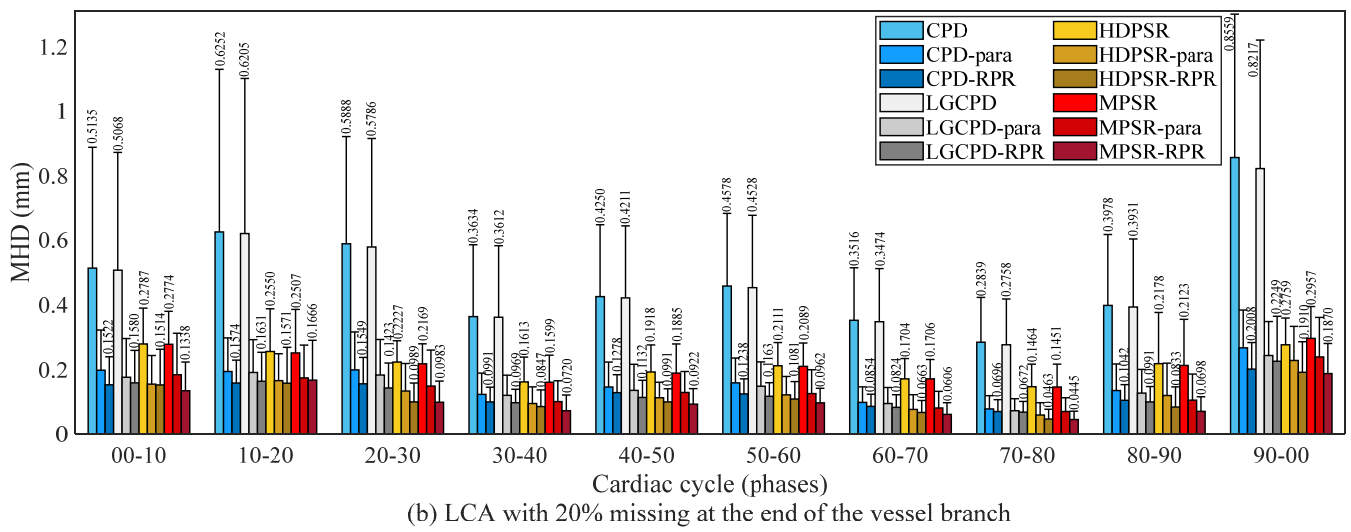

(b) LCA with 20% missing at the end of the vessel branch

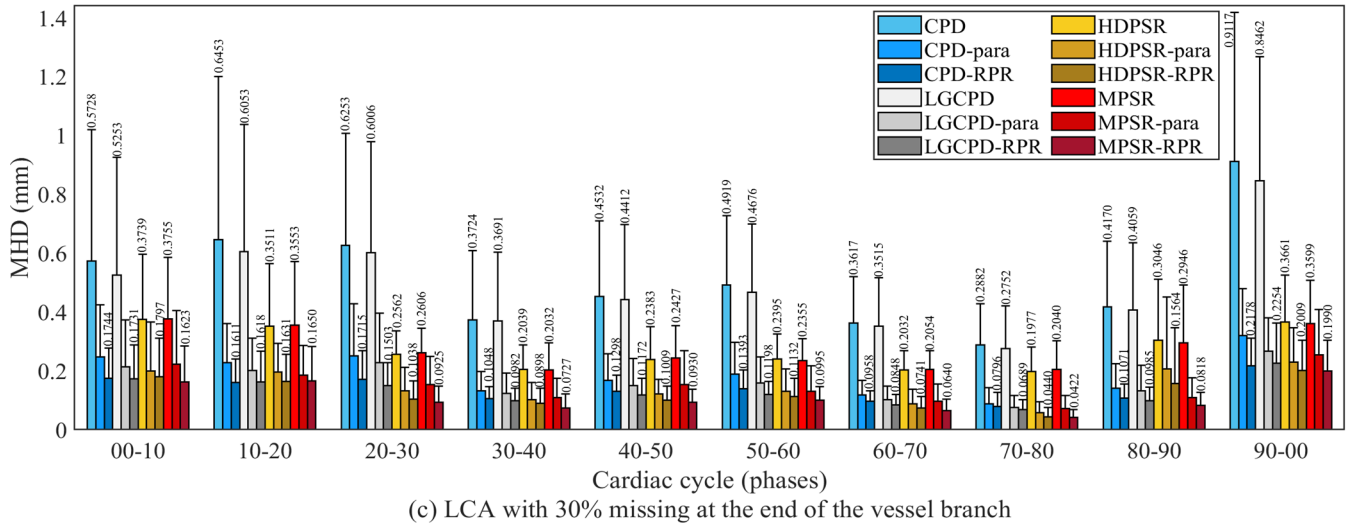

(c) LCA with 30% missing at the end of the vessel branch

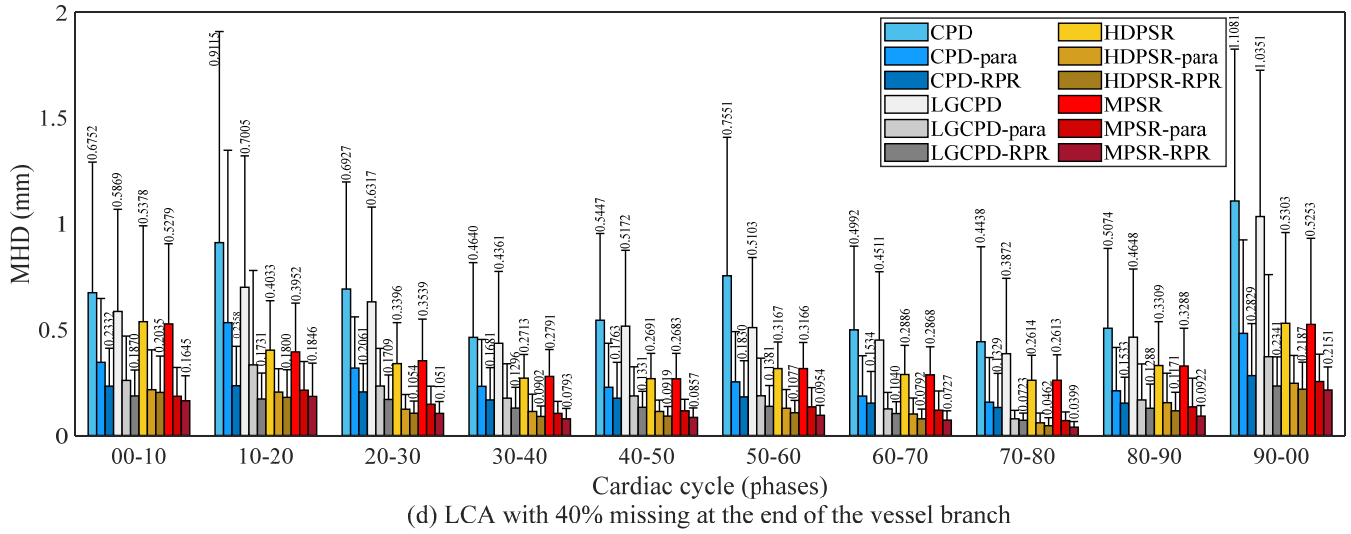

(d) LCA with 40% missing at the end of the vessel branch

Fig. 6. MHD for LCA with different degrees of missing data. The bar represents the average value of MHD for 16 data and the black line on the bar denotes the corresponding standard deviation.

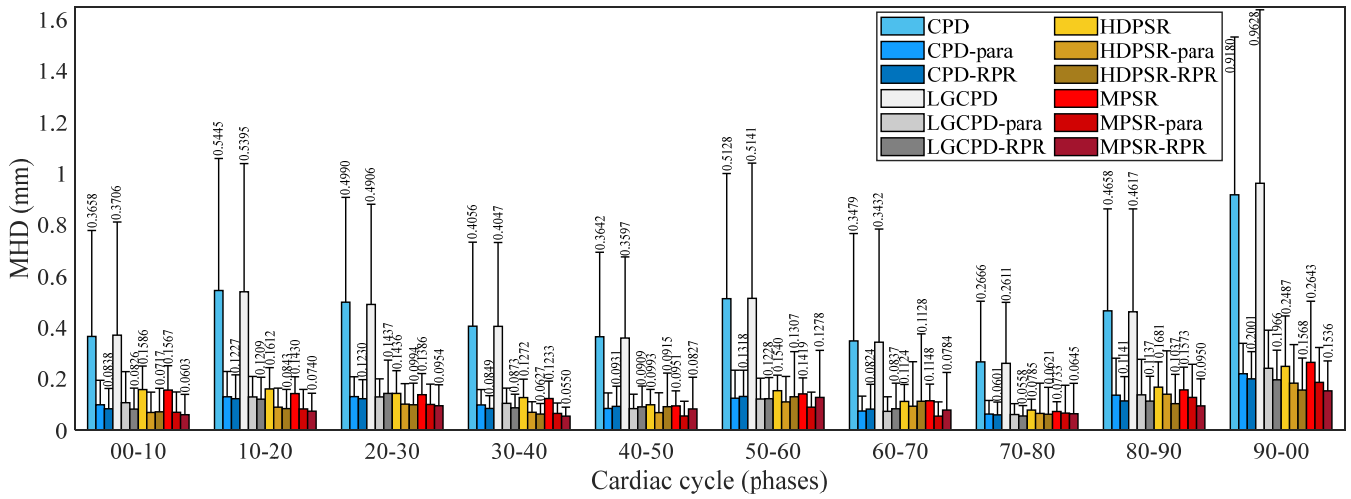

(a) RCA with 10% missing at the end of the vessel branch

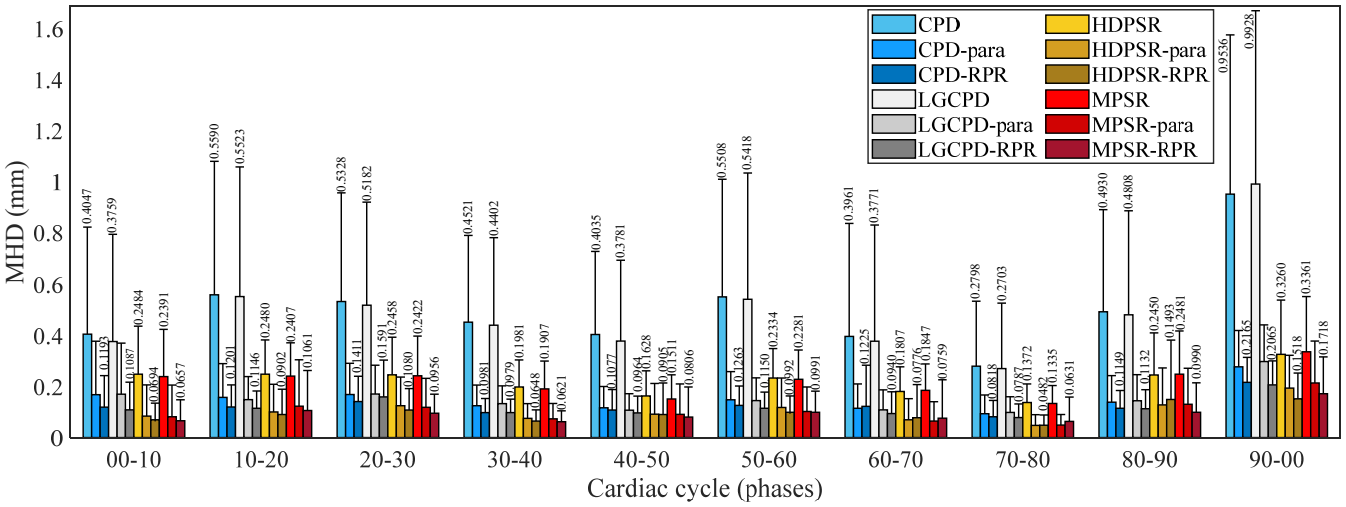

(b) RCA with 20% missing at the end of the vessel branch

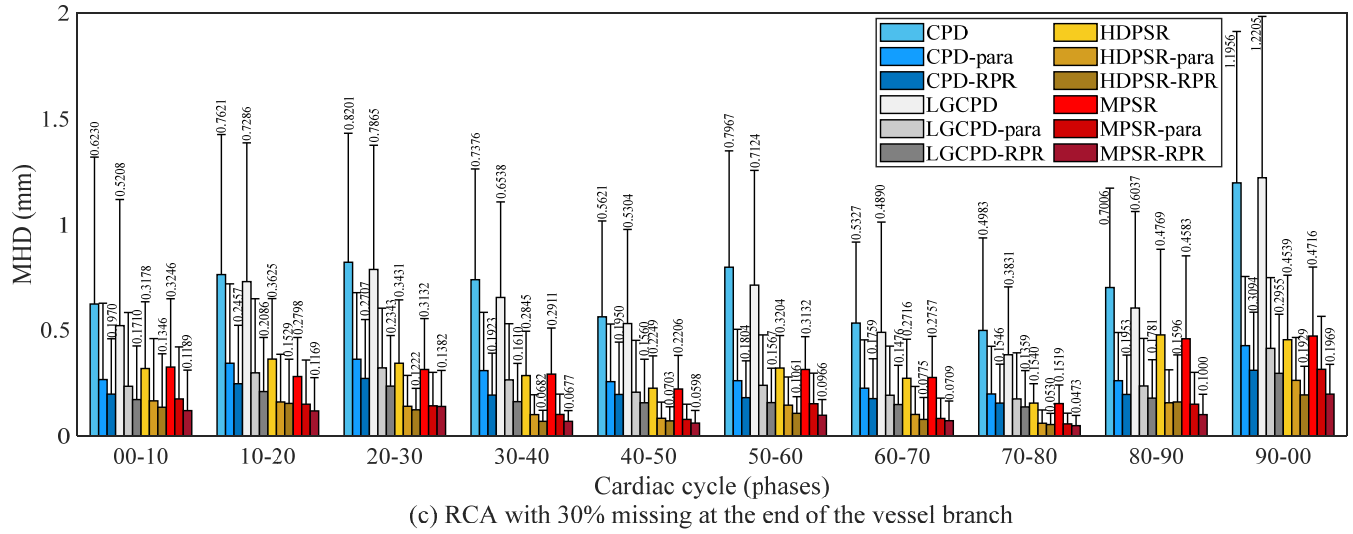

(c) RCA with 30% missing at the end of the vessel branch

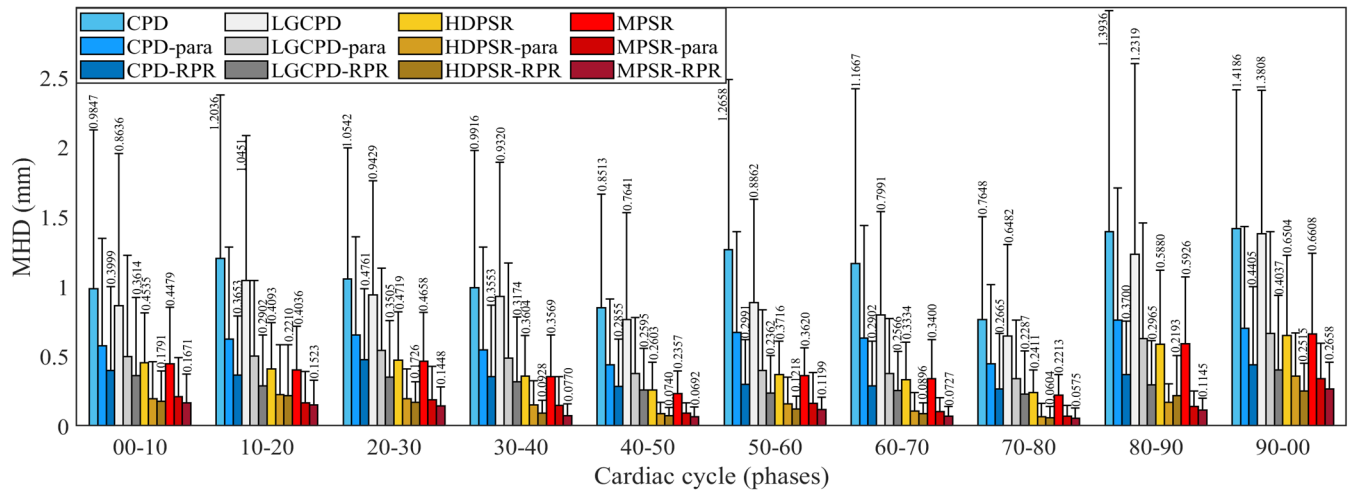

(d) RCA with 40% missing at the end of the vessel branch

Fig. 7. MHD for RCA with different degrees of missing data. The bar represents the average value of MHD for 16 data and the black line on the bar denotes the corresponding standard deviation.

both LCA and RCA. After using the removal strategy, the MHD value was further decreased. For the LCA with 10% missing, the removal strategy helped the CPD method reduce the MHD mean value. The range of the reduction was 0.2050 to 0.6231. Similarly, the strategy aided the LGCPD algorithm in reducing the MHD mean value, within the range of 0.2043 to 0.6044. The HDPSR and MPSR approaches achieved reductions within the range of 0.0167 to 0.0655 and 0.0183 to 0.0665, respectively. As the missing degree increased, the effect of the removal strategy became more pronounced. For the LCA with 40% missing, the removal strategy helped the CPD method reduce the MHD mean value within the range of 0.2959 to 0.8252, while for the LGCPD algorithm, the range was 0.3065 to 0.8010. In the case of the HDPSR and MPSR algorithms, the range of the reduction was 0.1772 to 0.3343 and 0.1826 to 0.3634, respectively. A similar observation was made for the RCA. These results confirmed the effectiveness of the removal strategy. Furthermore, for the LCA with 40% missing, the MPSR-RPR algorithm achieved a significantly lower mean value of the MHD in comparison with the existing CPD, LGCPD, and HDPSR methods. The range of the deceased MHD mean values were 0.3847 to 0.8930, 0.3473 to 0.8200, and 0.1834 to 0.3733, respectively for the three comparisons. Similar results were obtained for the RCA with 40% missing data, with the corresponding ranges of 0.7073 to 1.2791, 0.5907 to 1.1174, and 0.1836 to 0.4735, respectively. The numerical results that support the above ranges are presented in Fig. 6 and Fig. 7.

Tab. 2 and Tab. 3 list the total running time for the 16 data of the LCA and RCA, respectively. It can be seen that, in the same kind of method (e.g., CPD, CPD-para, and CPD-RPR), the running time of the algorithm with redundant point removal is the shortest.

Fig. 8 and Fig. 9 show the performance of the MPSR-RPR method for matching two centerline point sets between adjacent phases. It can be seen that, on the whole, the moving point set coincides well with the ground truth point set after the registration for both the LCA and the RCA during the whole cardiac cycle. However, at the end of the vessel branch, there are still some mismatch problems because the redundant points are deleted too much or not completely, as shown in the second column of the fourth row (i.e., green circle) in Fig. 8.

Tab. 2. The total running time (s) of 16 data for the LCA

	10% missing	20% missing	30% missing	40% missing
CPD	193.5892	192.4055	189.5788	172.3934
CPD-para	193.6610	183.8690	184.4042	172.8440
CPD-RPR	**173.1613**	**170.3821**	**166.8610**	**150.4044**
LGCPD	199.2881	198.7452	191.1487	181.5343
LGCPD-para	194.9297	192.9477	185.2232	177.1199
LGCPD-RPR	**187.7787**	**187.0101**	**169.9318**	**153.9296**
HDPSR	3724.4868	3951.8949	3742.9641	3202.7314
HDPSR-para	3863.0144	4167.1729	4093.5676	3896.3061
HDPSR-RPR	**2788.8520**	**2960.3535**	**3288.5781**	**2810.4066**
MPSR	2748.9119	4154.0572	3966.8349	3080.7381
MPSR-para	3307.2952	3693.3297	3700.5656	3524.5469
MPSR-RPR	**2712.7141**	**2893.0494**	**2729.3459**	**2361.0943**

Tab. 3. The total running time (s) of 16 data for the RCA

	10% missing	20% missing	30% missing	40% missing
CPD	129.5427	118.1398	118.7873	115.8133
CPD-para	124.7330	116.1415	113.9543	103.8917
CPD-RPR	**106.5017**	**104.8382**	**98.8544**	**97.3321**
LGCPD	126.5910	118.4211	106.0735	114.3632
LGCPD-para	119.0496	117.1059	106.7356	106.0529
LGCPD-RPR	**106.8672**	**105.8673**	**101.0042**	**99.4965**
HDPSR	1469.4228	1283.0165	1350.7754	1221.6019
HDPSR-para	1311.3518	1285.7463	1308.1285	1289.0941
HDPSR-RPR	**945.3440**	**898.0592**	**969.9684**	**972.6587**
MPSR	1069.4416	1568.8709	1599.1575	1117.8734
MPSR-para	1092.3702	1114.3485	1073.6332	1144.4117
MPSR-RPR	**978.3677**	**963.0564**	**871.5041**	**861.4177**

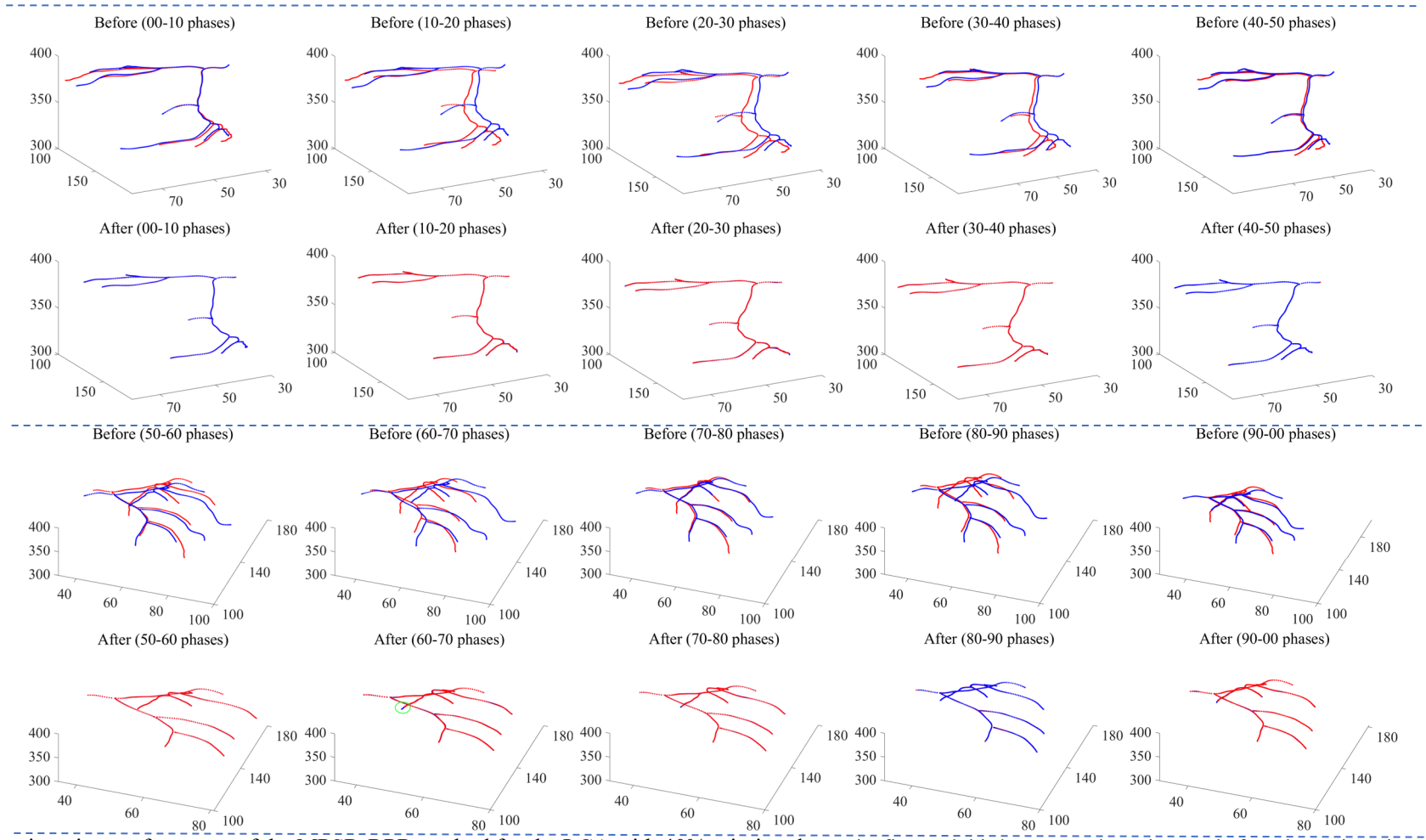

Fig. 8. The registration performance of the MPSR-RPR method for the LCA with 40% missing data. The first and third rows are the point sets before the registration, and the blue point set is the moving point set and the red one denotes the target point set. The second and fourth rows denote the point sets after the registration, and the blue point set is the moving point set and the red one represents the point set of ground truth. The green circle shows inaccurate registration.

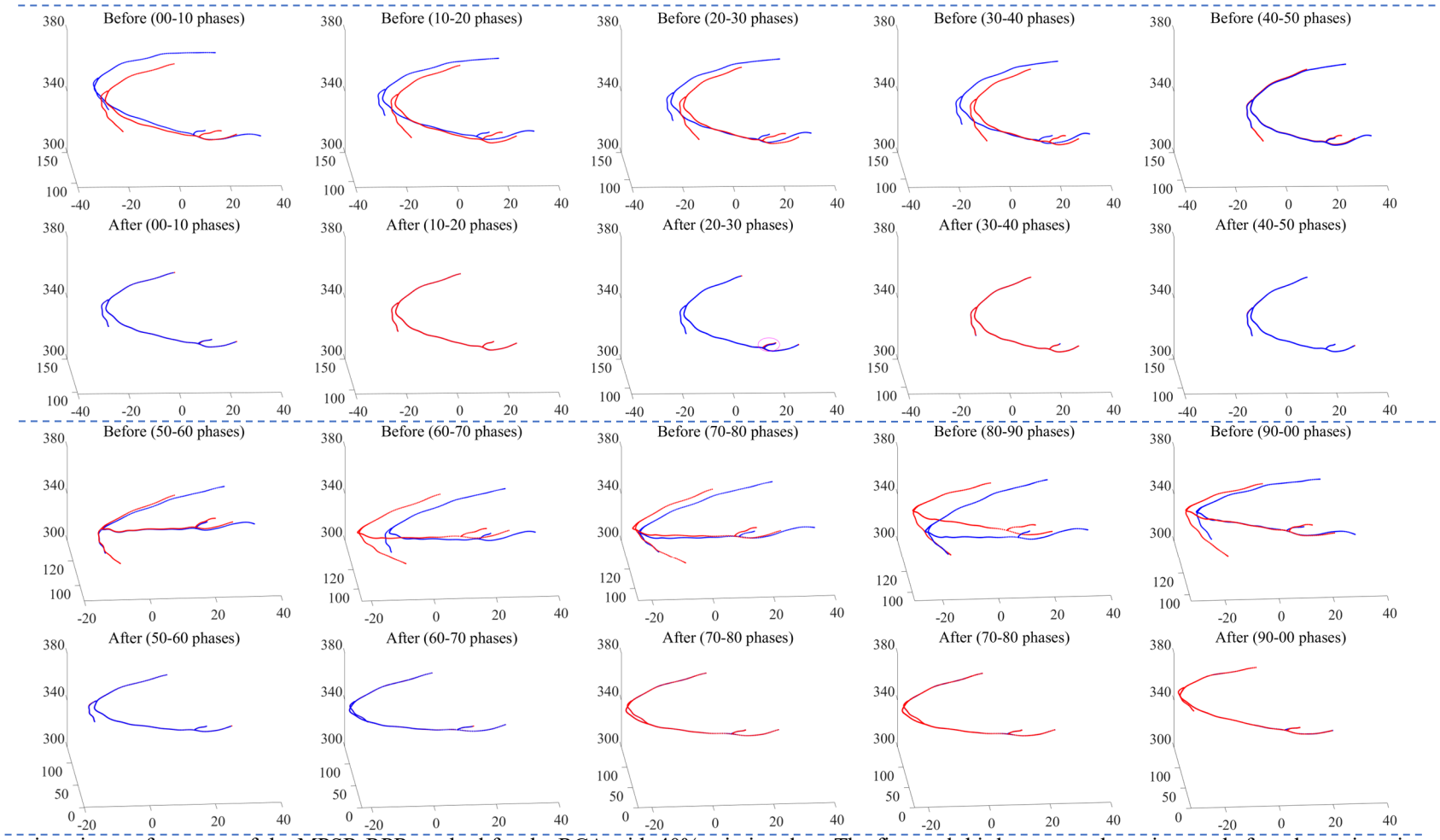

Fig. 9. The registration performance of the MPSR-RPR method for the RCA with 40% missing data. The first and third rows are the point sets before the registration, and the blue point set is the moving point set and the red one denotes the target point set. The second and fourth rows denote the point sets after the registration, and the blue point set is the moving point set and the red one represents the point set of ground truth. The pink circle shows inaccurate alignment.

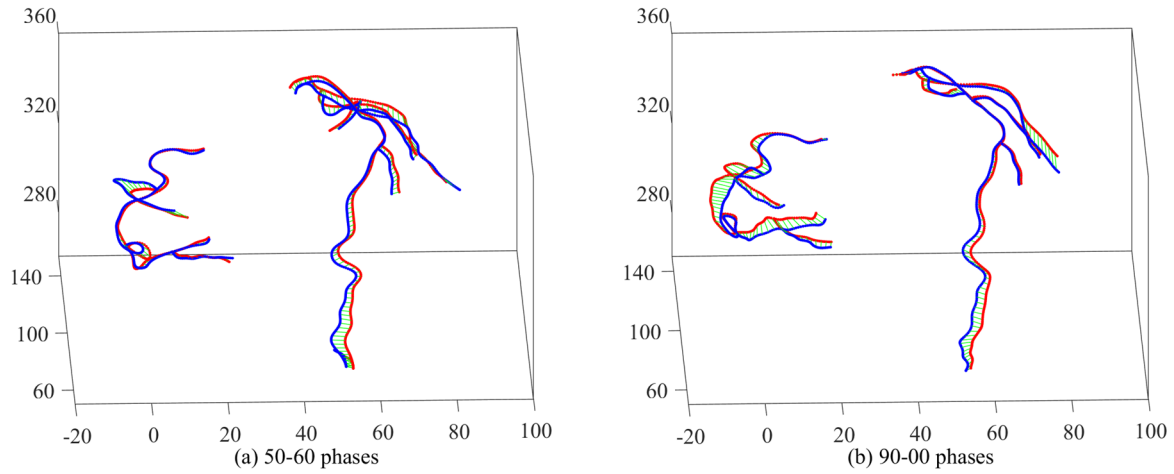

Fig. 10. The trajectory (green line) of the real vessels between the different phases.

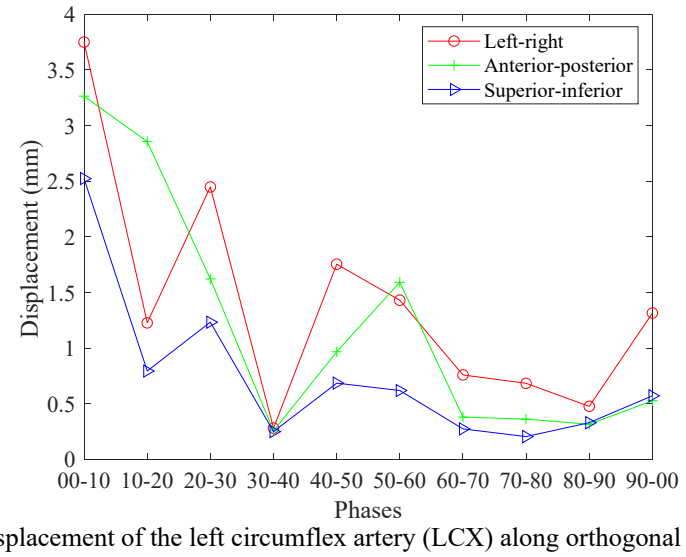

Fig. 11. Displacement of the left circumflex artery (LCX) along orthogonal axes for one subject.

The motion trajectory for a real vessel obtained by the MPSR-RPR method is shown in Fig. 10. Fig. 11 shows the displacement of the LCX along different directions. From Fig. 11, it can be known that the displacement of LCX is predominantly in the Left-right direction. The first trough around the 30-40 phase corresponds to the end of the systole of the heart, and the second trough around the 70-80 phase corresponds to the end of the diastole of the heart [5].

5. Discussion

This study aimed to address the challenges of aligning coronary arteries with missing data. Our results demonstrated that as the missing percentage on the vessel increases, the registration accuracy of the existing algorithm (e.g., the CPD method) decreases. This can be explained from the perspective of the likelihood function [30]. When the redundant points are present in the moving point set, in order to achieve a small negative log-likelihood function, the redundant points are squeezed to the point-rich regions in the target point set rather than to the missing point area. Conversely, when missing points are present in the moving point set, to minimize the negative log-likelihood function, the points near the missing data are elongated toward regions with the redundant point in the target point set. This unjustified squeezing or elongating in the moving point set can lead to a decrease in registration accuracy, as shown in Fig. 1. Therefore, the removal of redundant points becomes necessary.

To overcome the challenge, the study proposed a multi-constraint point set registration with the redundant point removal method for aligning coronary arteries. From Fig. 6 and Fig. 7, it can be concluded that the performance of the CPD approach exhibited the poorest performance among all methods. This can be attributed to the fact that the CPD method solely relied on the MCT as the constraint. In contrast, the LGCPD algorithm incorporated MCT as a global constraint and leveraged landmark point pairs information of vessels as an additional constraint, resulting in improved performance than the CPD approach. In addition to MCT and bifurcation point information, the MPSR algorithm integrated shape context and nearest neighbor information of the point set as the local structure constraint. This led to significant improvement in performance compared to the LGCPD method. The smoothing regularization parameter λ and the Gaussian filter width β were optimized to control the fit degree of the two point sets during the alignment process. With these two parameters changing in the registration, the MHD mean value can be reduced. Based on the MPSR algorithm, the proposed MPSR-RPR approach reduced the impact of missing points by the designed removal strategy, therefore, achieving the best performance among the different methods. Furthermore, the proposed removal strategy was also inserted into the existing CPD, LGCPD, and HDPSR methods, resulting in a significant enhancement in their registration performance, highlighting the robustness and effectiveness of the proposed method. It is worth noting that, because the simulation data were highly dependent on the motion and deformation degree of the real data, in Fig. 6 and Fig. 7, two troughs are observed. The first trough is around the 30-40 (or 40-50) phases, while the second one is around the 70-80 phases, representing the end of the systole and the end of the diastole of the heart, respectively. As shown in Tab. 2 and Tab. 3, although the geometric structure information of the vessel was utilized in the redundant point removal process, it did not increase the running time of the algorithm. On the contrary, due to the reduction of the number of points, the computation time of the alignment approach with redundant point removal was the shortest among methods of the same kind, for both the LCA and RCA.

There are, however, some limitations associated with the MPSR-RPR algorithm. Firstly, the performance of the method is dependent on the selection of registration parameters, e.g., λ_{tough}, β_{tough}. The grid traversal method was adopted to search for these optimal parameters. Nevertheless, since the deformation and displacement degrees vary for each pair of point sets to be aligned, these fixed optimal parameters may not yield the best results for all the point set pairs requiring alignment. Secondly, the real centerlines of the vessels were obtained by the semi-automatic method that requires manual intervention.

In the future, it would be beneficial to explore an adaptive parameter that takes into account the structure of the point set. Additionally, the integration of automatic vessel segmentation [31] and centerline tracking [32] methods could help reduce the manual burden involved in obtaining the real centerlines of vessels.

6. Conclusion

The issue of missing data can significantly affect the registration accuracy of coronary arteries. This paper proposed a new non-rigid point set registration algorithm to tackle this challenge. Our proposed method incorporates various constraints, including the moving coherent, local

features, and the corresponding relationship between bifurcation point pairs, to enhance the matching process. Additionally, an automatic removal strategy was designed to mitigate the effects of missing points. Experiment results demonstrated that our proposed approach achieved higher registration accuracy than the other existing approaches when dealing with vessels containing different degrees of missing data. These promising findings suggest that the proposed method is suitable for registering coronary artery point sets and has the potential to be used in the registration of other vessels, such as the cerebral and liver vessels, where missing data may also be present at the end of the vessel branches.

Acknowledgments

This work was supported by the National Natural Science Foundation of China (No. 62273082, and No. 61773110), the Natural Science Foundation of Liaoning Province (No. 20170540312, and No. 2021-YGJC-14), the Liaoning Provincial "Selecting the Best Candidates by Opening Competition Mechanism" Science and Technology Program (No. 2022JH1/10400004), the Basic Scientific Research Project (Key Project) of Liaoning Provincial Department of Education (LJKZ00042021), and Fundamental Research Funds for the Central Universities (No. N2119008). This work was also supported by the Shenyang Science and Technology Plan Fund (No. 21-104-1-24, No. 20-201-4-10, and No. 201375).

Declaration of competing interest

The authors declare that they have no conflict of interest.

List of abbreviations

CAD	Coronary artery disease
ICP	Iterated close point
MLE	Maximum likelihood estimation
MPSR-RPR	Multi-constraint point set registration with redundant point removal
MHD	Modified Hausdorff distance
GMM	Gaussian mixture model
CPD	Coherent point drift
MCT	Motion coherence theory
LGCPD	Landmark-guided coherent point drift
EM	Expectation-maximization
PSSM	Point set similarity model
HDPSR	Hausdorff-distance-guided point set registration
CCTA	Coronary computed tomography angiography
MPSR	Multi-constraint Point Set Registration
CPD-RPR	Coherent point drift with redundant point removal
LGCPD-RPR	Landmark-guided coherent point drift with redundant point removal
HDPSR-RPR	Hausdorff-distance-guided point set registration with redundant point removal
CPD-para	Coherent point drift with only changed registration parameters
LGCPD-para	Landmark-guided coherent point drift with only changed registration parameters
HDPSR-para	Hausdorff-distance-guided point set registration with only changed registration parameters
MPSR-para	Multi-constraint point set registration with only changed registration parameters
LCX	Left circumflex artery

References

[1] R.S. Vasan, D.M. Enserro, V. Xanthakis, A.S. Beiser, S. Seshadri, Temporal Trends in the Remaining Lifetime Risk of Cardiovascular Disease Among Middle-Aged Adults Across 6 Decades: The Framingham Study, Circulation. 145 (2022) 1324-1338. https://doi.org/10.1161/CIRCULATIONAHA.121.057889.

[2] S.M. Pinto Pereira, R. Shafran, M.D. Nugawela, L. Panagi, D. Hargreaves, S.N. Ladhani, S.D. Bennett, S.M. Pinto Pereira, R. Shafran, M.D. Nugawela, Discovery and systematic characterization of risk variants and genes for coronary artery disease in over a million participants., Nat. Genet. (2022) 1-13. https://doi.org/10.1038/s41588-022-01233-6.

[3] J. Puentes, C. Roux, M. Garreau, J.-L. Coatrieux, Dynamic feature extraction of coronary artery motion using DSA image sequences, IEEE Trans. Med. Imaging. 17 (1998) 857-871. https://doi.org/10.1109/42.746619.

[4] A.A. Young, P.J. Hunter, B.H. Smaill, Estimation of epicardial strain using the motions of coronary bifurcations in biplane cineangiography, IEEE Trans. Biomed. Eng. 39 (1992) 526-531. https://doi.org/10.1109/10.135547.

[5] G. Yang, J. Zhou, D. Boulmier, M.-P. Garcia, L. Luo, C. Toumoulin, Characterization of 3-D coronary tree motion from MSCT angiography, IEEE Trans. Inf. Technol. Biomed. 14 (2010) 101-106. https://doi.org/10.1109/TITB.2009.2032333.

[6] S. Habert, P. Khurd, C. Chefd'Hotel, Registration of multiple temporally related point sets using a novel variant of the coherent point drift algorithm: application to coronary tree matching, in: Med. Imaging 2013 Image Process., International Society for Optics and Photonics, 2013: p. 86690M. https://doi.org/10.1117/12.2004764.

[7] B. Xu, B. Yang, J. Xiao, A. Song, B. Wang, L. Wang, L. Xu, S.E. Greenwald, Y. Yao, Estimation of coronary artery movement using a non-rigid registration with global-local structure preservation, Comput. Biol. Med. 141 (2022) 105125. https://doi.org/10.1016/j.compbiomed.2021.105125.

[8] G. Yang, A. Broersen, R. Petr, P. Kitslaar, M.A. de Graaf, J.J. Bax, J.H.C. Reiber, J. Dijkstra, Automatic coronary artery tree labeling in coronary computed tomographic angiography datasets, in: 2011 Comput. Cardiol., IEEE, 2011: pp. 109-112. https://doi.org/10.1007/s12471-010-0047-3.

[9] Q. Cao, A. Broersen, P.H. Kitslaar, M. Yuan, B.P.F. Lelieveldt, J. Dijkstra, Automatic coronary artery plaque thickness comparison between baseline and follow-up CCTA images, Med. Phys. 47 (2020) 1083-1093. https://doi.org/10.1002/mp.13993.

[10] P.J. Besl, N.D. McKay, A method for registration of 3-D shapes, IEEE Trans. Pattern Anal. Mach. Intell. 14 (1992) 239-256. https://doi.org/10.1109/34.121791.

[11] A.W. Fitzgibbon, Robust registration of 2D and 3D point sets, Image Vis. Comput. 21 (2003) 1145-1153. https://doi.org/10.1016/j.imavis.2003.09.004.

[12] J. Yang, H. Li, D. Campbell, Y. Jia, Go-ICP: A Globally Optimal Solution to 3D ICP Point-Set Registration, IEEE Trans. Pattern Anal. Mach. Intell. 38 (2016) 2241-2254. https://doi.org/10.1109/TPAMI.2015.2513405.

[13] A. Myronenko, X. Song, M. Carreira-Perpinan, Non-rigid point set registration: Coherent point drift, Adv. Neural Inf. Process. Syst. 19 (2006) 1009-1016. https://ieeexplore.ieee.org/document/6287458?denied= (accessed December 14, 2020).

[14] A. Myronenko, X. Song, Point set registration: Coherent point drift, IEEE Trans. Pattern Anal. Mach. Intell. 32 (2010) 2262-2275. https://doi.org/10.1109/TPAMI.2010.46.

[15] A.L. Yuille, N.M. Grzywacz, A mathematical analysis of the motion coherence theory, Int. J. Comput. Vis. 3 (1989) 155-175. https://doi.org/10.1007/BF00126430.

[16] Y. Hu, E.-J. Rijkhorst, R. Manber, D. Hawkes, D. Barratt, Deformable vessel-based registration using landmark-guided coherent point drift, in: Int. Work. Med. Imaging Virtual Real., Springer, 2010: pp. 60–69. https://doi.org/10.1007/978-3-642-15699-1_7.

[17] Y. Liu, H. Cao, Y. Zhao, Q. He, Y. Yang, L. Wang, G. Lin, J. Zhou, A Remote sensing image registration algorithm based on multiple constraints and a variational Bayesian framework, Remote Sens. Lett. 12 (2021) 296-305. https://doi.org/10.1080/2150704X.2021.1884916.

[18] S. Ge, G. Fan, Topology-aware non-rigid point set registration via global–local topology preservation, Mach. Vis. Appl. 30 (2019) 717-735. https://doi.org/10.1007/s00138-019-01024-w.

[19] Q.-Y. Chen, D.-Z. Feng, H.-S. Hu, A robust non-rigid point set registration algorithm using both local and global constraints, Vis. Comput. (2022) 1-18. https://doi.org/10.1007/s00371-022-02400-w.

[20] G. Wang, Z. Wang, Y. Chen, Q. Zhou, W. Zhao, Context-aware Gaussian fields for non-rigid point set registration, in: Proc. IEEE Conf. Comput. Vis. Pattern Recognit., 2016: pp. 5811-5819. https://doi.org/10.1109/CVPR.2016.626

[21] S. Yoon, C.H. Yoon, D. Lee, Topological recovery for non-rigid 2D/3D registration of coronary artery models, Comput. Methods Programs Biomed. 200 (2021) 105922. https://doi.org/10.1016/j.cmpb.2020.105922.

[22] T. Park, S. Khang, H. Jeong, K. Koo, J. Lee, J. Shin, H.C. Kang, Deep learning segmentation in 2d x-ray images and non-rigid registration in multi-modality images of coronary arteries, Diagnostics. 12 (2022) 778. https://doi.org/10.3390/diagnostics12040778.

[23] M. Wang, 3D coronary artery elastic registration based on differential invariant signatures, Comput. Methods Biomech. Biomed. Engin. Imaging Vis. 10 (2022) 622-632. https://doi.org/10.1080/21681163.2021.2018046.

[24] S. Zeng, J. Feng, Y. An, B. Lu, J. Lu, J. Zhou, Towards Accurate and Complete Registration of Coronary Arteries in CTA Images, in: Int. Conf. Med. Image Comput. Comput. Interv., Springer, 2018: pp. 419-427. https://doi.org/10.1007/978-3-030-00934-2_47.

[25] S. Bayer, N. Ravikumar, M. Strumia, X. Tong, Y. Gao, M. Ostermeier, R. Fahrig, A. Maier, Intraoperative brain shift compensation using a hybrid mixture model, in: Int. Conf. Med. Image Comput. Comput. Interv., Springer, 2018: pp. 116-124. https://doi.org/10.1007/978-3-030-00937-3_14.

[26] J. Ma, J. Zhao, A.L. Yuille, Non-rigid point set registration by preserving global and local structures, IEEE Trans. Image Process. 25 (2016) 53-64. https://doi.org/10.1109/TIP.2015.2467217.

[27] D.-J. Kroon, Segmentation of the mandibular canal in cone-beam CT data., Citeseer, 2011. https://doi.org/10.3990/1.9789036532808.

[28] F.L. Bookstein, Principal warps: Thin-plate splines and the decomposition of deformations, IEEE Trans. Pattern Anal. Mach. Intell. 11 (1989) 567-585. https://doi.org/10.1109/34.24792.

[29] M.-P. Dubuisson, A.K. Jain, A modified Hausdorff distance for object matching, in: Proc. 12th Int. Conf. Pattern Recognit., IEEE, 1994: pp. 566-568. https://doi.org/10.1109/ICPR.1994.576361.

[30] T. Tang, M. Tomizuka, Track deformable objects from point clouds with structure preserved registration, Int. J. Rob. Res. (2019). https://doi.org/10.1177/0278364919841431.

[31] A. Song, L. Xu, L. Wang, B. Wang, X. Yang, B. Xu, B. Yang, S.E. Greenwald, Automatic coronary artery segmentation of CCTA images with an efficient feature-fusion-and-rectification 3D-UNet, IEEE J. Biomed. Heal. Informatics. 26 (2022) 4044-4055. https://doi.org/10.1109/JBHI.2022.3169425.

[32] J.M. Wolterink, R.W. van Hamersvelt, M.A. Viergever, T. Leiner, I. Išgum, Coronary artery centerline extraction in cardiac CT angiography using a CNN-based orientation classifier, Med. Image Anal. 51 (2019) 46-60. https://doi.org/10.1016/j.media.2018.10.005.